Evaluation of the CCD camera for TFOSC, equipped with **Fairchild CCD 447BI**

Device ID E7256W4D5

Anton Norup Sørensen
Copenhagen University Observatory

May 2004

Contents

1 Introduction

This document contains a summary of the characterization results of a camera manufactured at Copenhagen University Observatory, equipped with the Fairchild CCD 447BI. This CCD has an imaging area of 2048 by 2048 pixels, each 15μm square. The detector is thinned and back-side illuminated. Two low noise outputs are used, which are called amplifier A and B in this report and in the user interface. These must be used individually. Another two amplifiers on the CCD, optimised for high speed readout, are not connected.

During the tests, the CCD substrate separated from its Kovar package, apparently due to stress from temperature changes. The CCD was returned to Fairchild and re-packaged. Testing after the re-packaging indicates that the detector is functioning normally. This report contains a combination of test results from before and after the re-packaging. In any areas where changes in performance could be expected, tests were repeated, and are in some cases compared to the previous results.

2 Cosmetics

Flat fields for the CCD at wavelengths of 1060nm, 550nm and 334nm are shown in the lower part of figures 1, 2 and 3, respectively.

In the central optical band, around 550nm, uniformity is very good, with a large scale structure of less than $\pm$1%. Most of the large variation seen is actually due to scattered light in the test setup. Spots with lower sensitivity are visible, of which two are quite large, but the area affected is less than 1% of the total surface.. Larger, circular spots are caused by grains on the window.

At the longest wavelengths, uniformity is poorer: In the majority of the field, large scale variations are at the $\pm$3% level, and near the edges the signal increases by about 10%. The 1060nm filter is relatively broad, with a FWHM of 30nm. Fringes are faintly visible, but will be more pronounced for more narrow band passes, as mentioned later. Reflections off the connecting electrodes are creating vertical bands.

At 334nm, uniformity is degraded relatively to the visual band. A vertical gradient of about 5% is present, and the appearance is more speckeled. In the centre on the low sensitivity spots, QE may be half of the surrounding area.

Charge traps and bad columns can be found by comparing a flat field exposure at very low illumination level to a well exposed one, as illustrated in figure 4. Here, several exposures at 50e^- and 65Ke^- were combined to produce two high S/N flat field maps for the comparison.

Defects found this way are described below. A deep trap will affect several pixels, as charge is moved through it during read-out. Only one clear detection of a trap was made, at coordinates (911,2009). Judging from the number of pixels affected, depth is around 500e^-. A handful of fainter traps were suspected, only affecting one or two pixels in the 50e^- flat field. From the complete absense of high-level traps and bad columns, and the very small number low-level traps, the cosmetic quality of the CCD in this respect is extremely good.

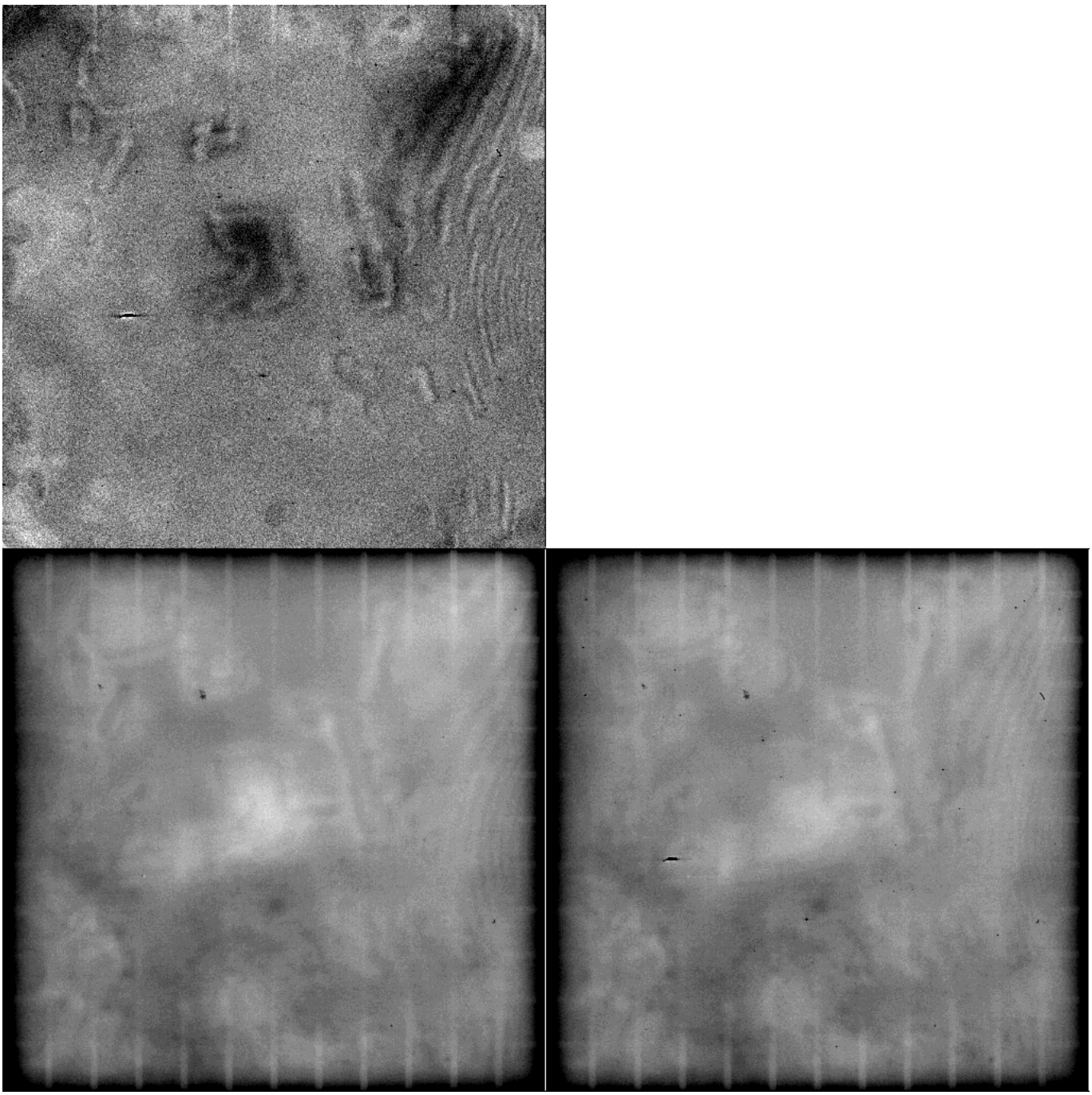

Figure 1: Flat field properties at 1060nm, recorded before the de-lamination incident. *Lower left:* The greyscale cuts are set to ±8% of the median level. *Lower right:* Four days later, with identical scaling. *Top:* Ratio between the two flat fields, displayed with cuts of ±2%.

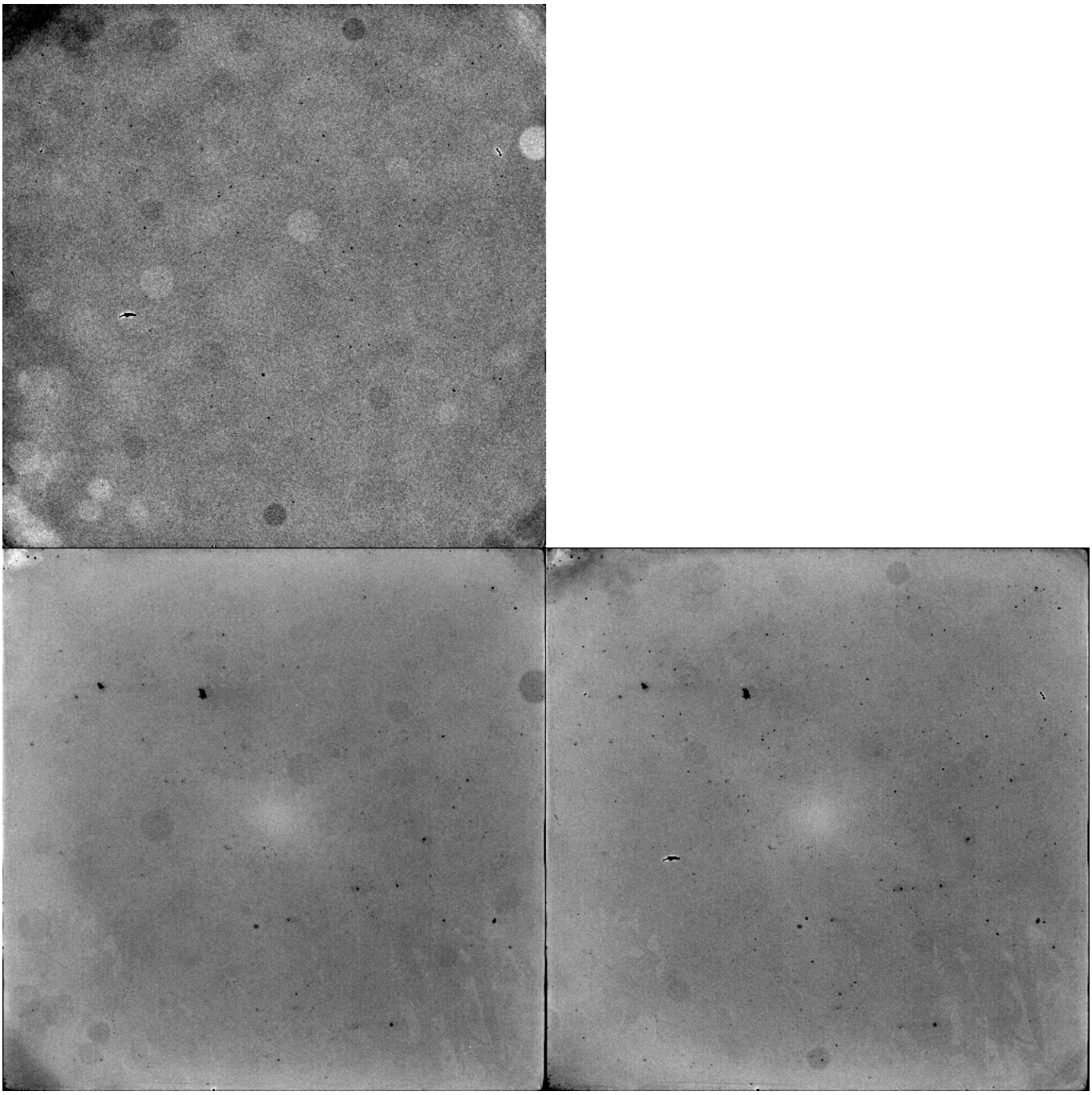

Figure 2: Flat field properties at 550nm. *Lower left:* The greyscale cuts are set to ±4% of the median level. *Lower right:* Four days later, with identical scaling. *Top:* Ratio between the two flat fields, displayed with cuts of ±2%. The change in the corners is caused by movement of a baffle in front of the camera.

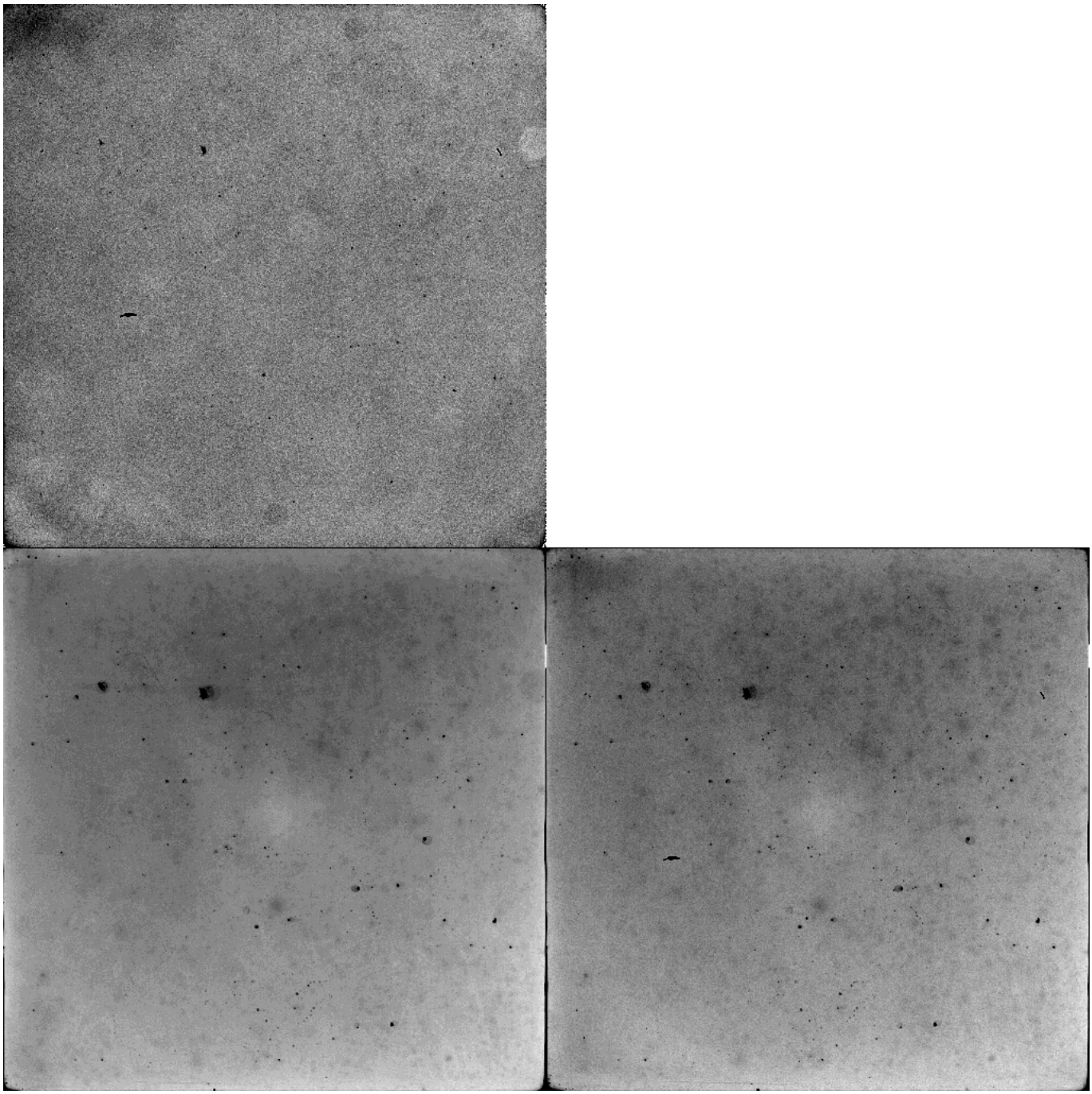

Figure 3: Flat field properties at 334nm. *Lower left:* The greyscale cuts are set to ±10% of the median level. *Lower right:* Two days later, with identical scaling. *Upper left:* Ratio between the two flat fields, displayed with cuts of ±4%.

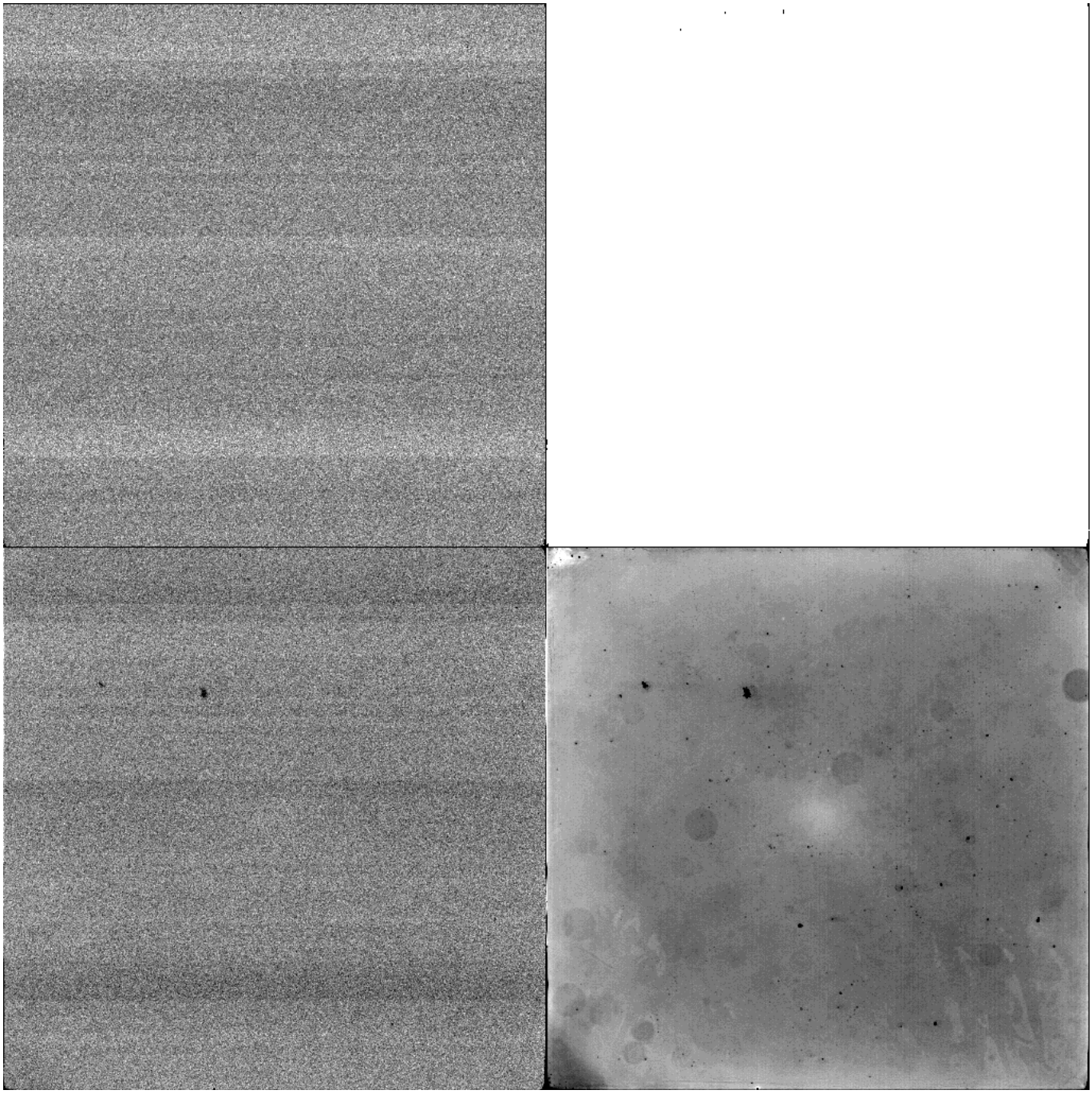

Figure 4: Comparison of a 550nm high and low illumination flat field, in order to identify charge traps. *Lower left:* Flat field at an illumination level of $50e^-$/pixel. Grey scale cuts are ± 15% of median level. Horisontal bands are from bias level instability, which was later damped considerably. *Lower right:* Flat field at an illumination level of $65.000e^-$/pixel. Grey scale cuts are ± 3% of median level. *Upper left:* Ratio of the two flat fields. Grey scale cuts are ± 15% of median level.

3 Gain, linearity and full-well

Gain, the conversion factor between Analog to digital units (ADU) and electrons was determined by analysis of photon noise statistics. The following conversion factors were found:

Gain	Amplifier A	Amplifier B
High gain	1.34e^-/ADU	1.35e^-/ADU
Low gain	5.02e^-/ADU	5.06e^-/ADU

Examples of gain determination from Poisson noise is shown in the upper part of figures 5, 6, 7 and 8. Here the gain is determined from the approximately constant level measured over a wide illumination range.

Gain determination from noise analysis is rarely precise enough for linearity measurements. In stead, linearity deviations are examined by measuring the ADU level versus exposure time, using a stable light source. Measurements made in this way are plotted in the lower half of the linearity figures.

By dividing the counts with the exposure time, corrected for shutter delay, a linear response should result in a constant level.

In high gain, linearity of amplifier A was found to be within ± 0.7% from 100e^- and up to digital saturation at 87Ke^-, and output B performs similarly with a deviation of ± 0.7% in the same interval. The linearity measurements around 100e^- should be regarded as somewhat uncertain, as error in bias level subtraction can have a large influence. See lower half of figures 5 and 6. Note that for both amplifiers, the Poisson gain measurements are too noisy for a precise linearity measurement.

In low gain, linearity of amplifiers A and B is within ± 0.7% from 100e^- to 150Ke^- or 30KADU. Above this, an abrupt increase in deviation indicate the onset of single pixel blooming full-well. See lower half of figure 7 and 8. The remaining low-gain digital range may be utilised when using binning.

In general, the linearity deviations found are quite significant. This is in part due to the timing and voltage setup chosen, as this was optimised for low read-out noise with less emphasis on linearity.

4 Read-out noise and bias frames

The CCD has two outputs low noise read-out, named amplifier A and B. Additional outputs for high speed readout exists, but are not connected.

The following table shows the read-out noise (RON) found in different amplifier configurations, at the fixed sampling rate of 60KHz:

	Amplifier A	Amplifier B
High gain:	5.1 e^-	5.3 e^-
Low gain:	7.6 e^-	7.8 e^-

In low gain mode, the coarse digital sampling is causing an increase in the effective read-out noise.

A bias frame, combined from six exposures from amplifier A is shown in figure 9. Faint horisontal bands are visible. These change randomly between images, and removal should be possible by tracking the vertical structure in the overscan region. An example of a vertical profile of a single bias frame is shown in figure 10. Variations with a peak-peak amplitude of about 1 e^- are visible.

The pressure sensor has been observed to create aditional noise, resulting i a periodic pattern across the image. This will effectively increase the RON to about 8 e^- in high gain. It is recommended to unplug the power to the pressure sensor while making science exposures.

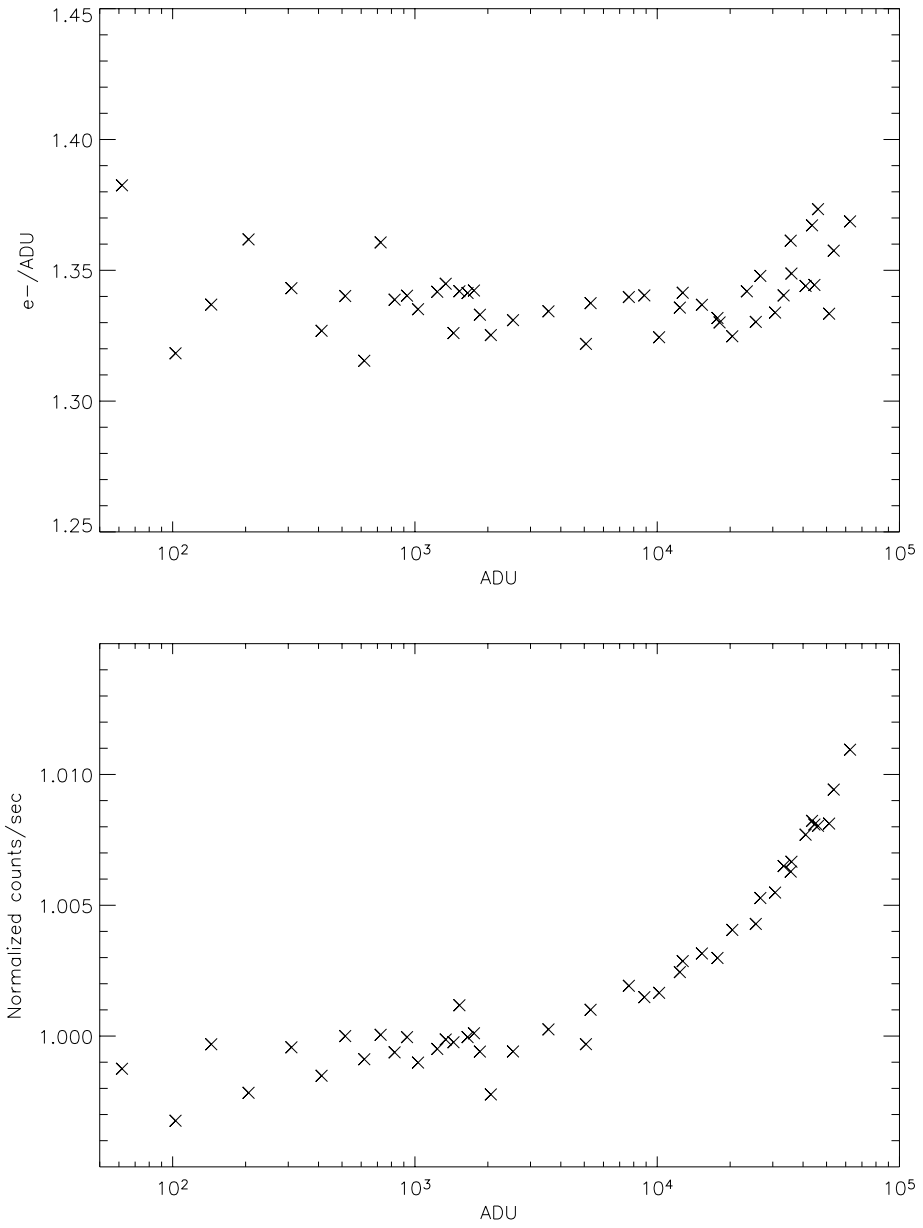

Figure 5: *Top:* Gain versus exposure level measured from noise statistics for amplifier A in high-gain mode. *Bottom:* A plot of ADU per second versus total exposure time, corrected for shutter delay.

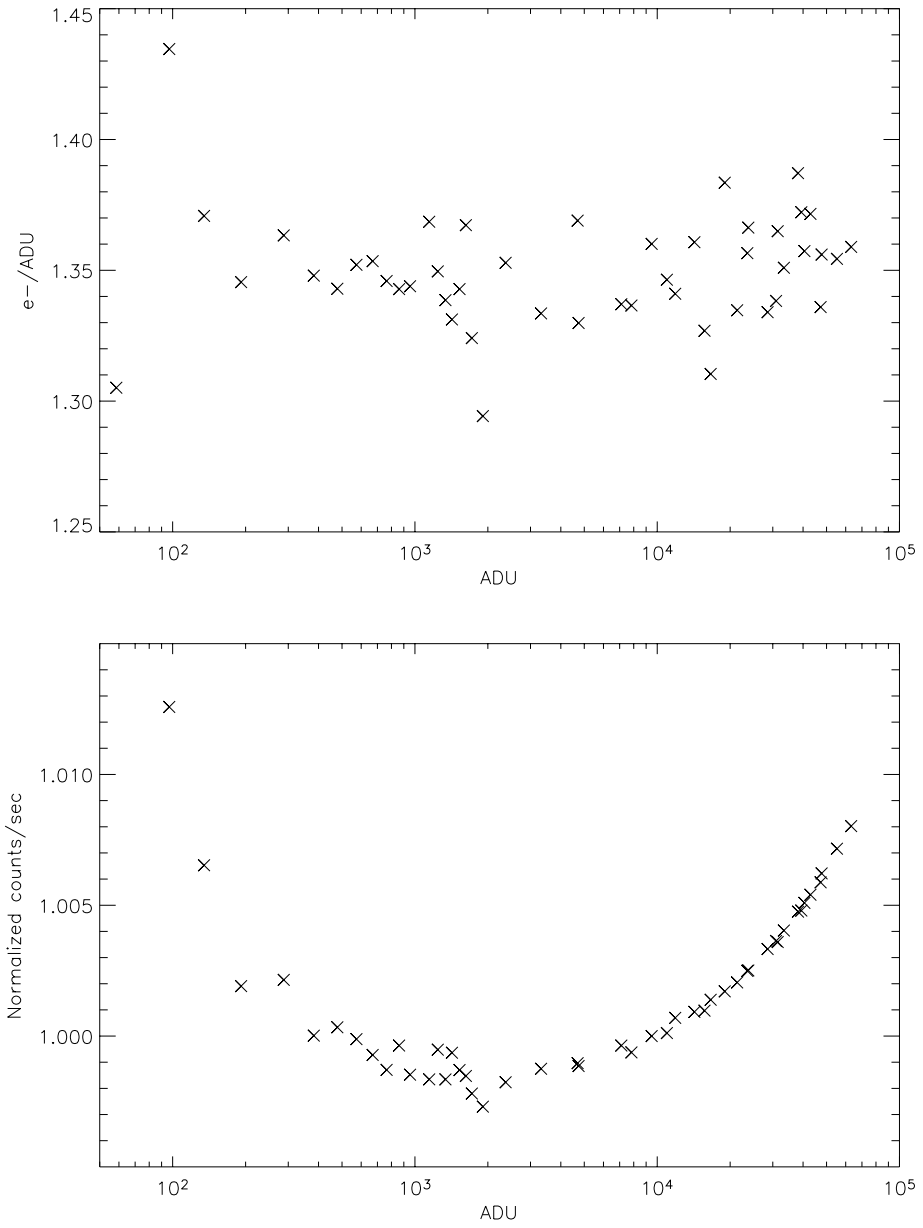

Figure 6: *Top:* Gain versus exposure level measured from noise statistics for amplifier B in high-gain mode. *Bottom:* A plot of ADU per second versus total exposure time, corrected for shutter delay.

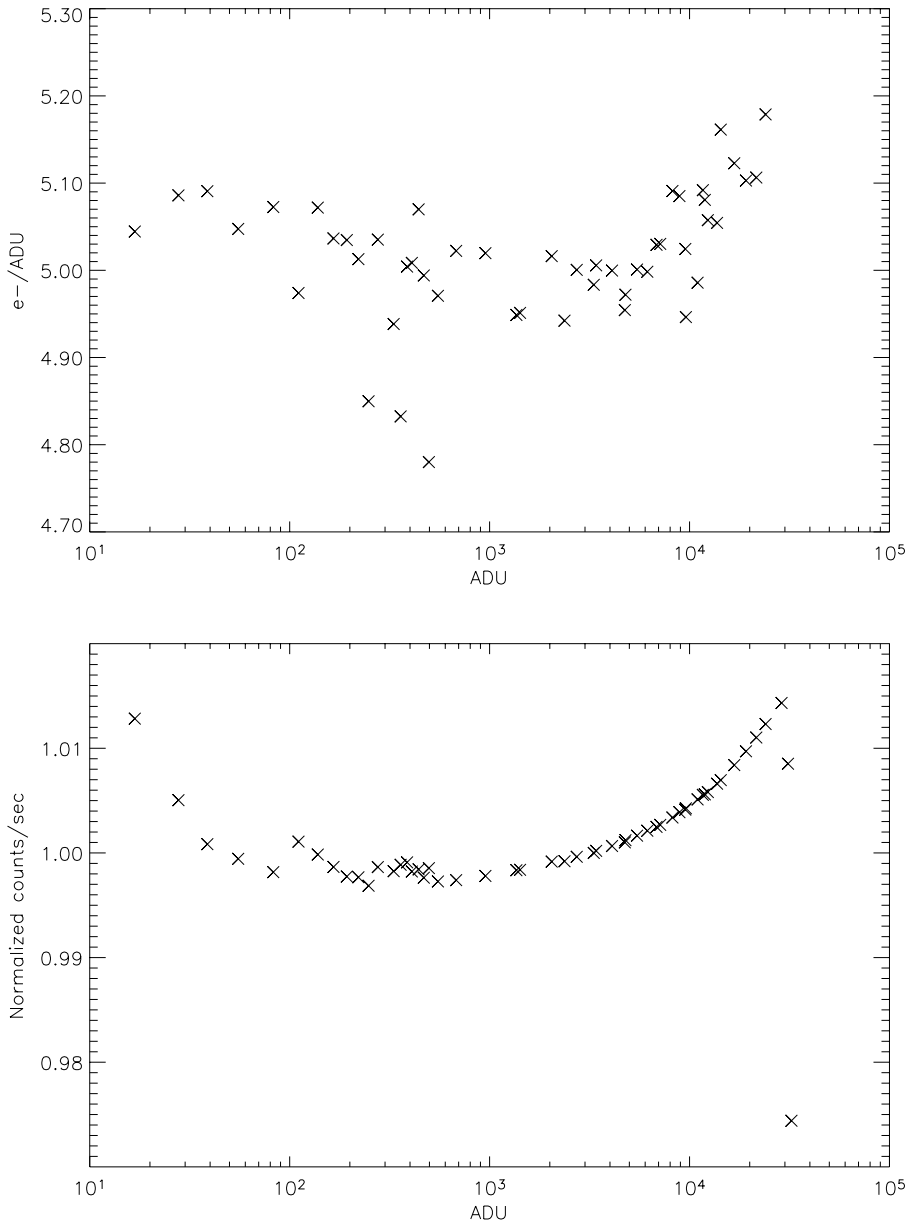

Figure 7: *Top:* Gain versus exposure level measured from noise statistics for amplifier A in low-gain mode. *Bottom:* A plot of ADU per second versus total exposure time, corrected for shutter delay.

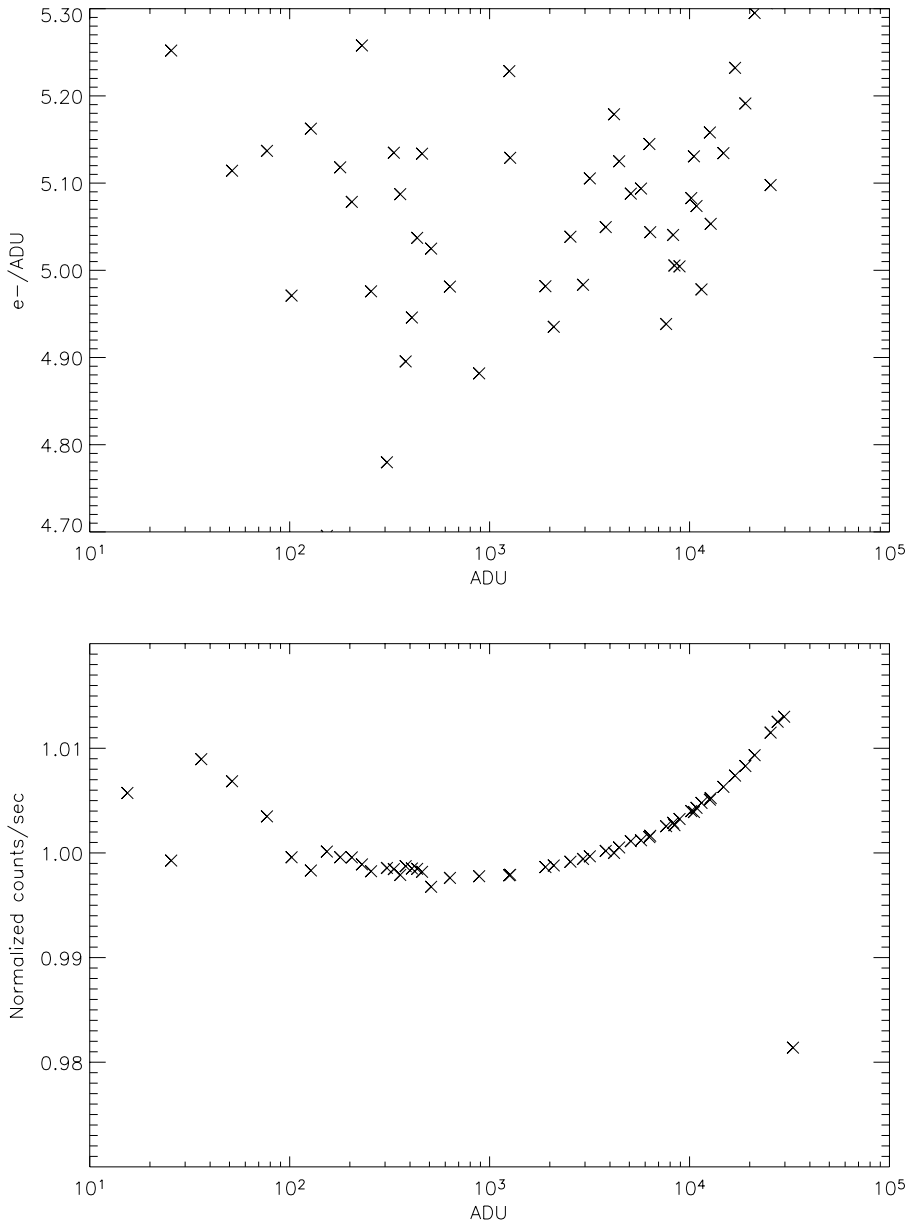

Figure 8: *Top:* Gain versus exposure level measured from noise statistics for amplifier B in low-gain mode. *Bottom:* A plot of ADU per second versus total exposure time, corrected for shutter delay.

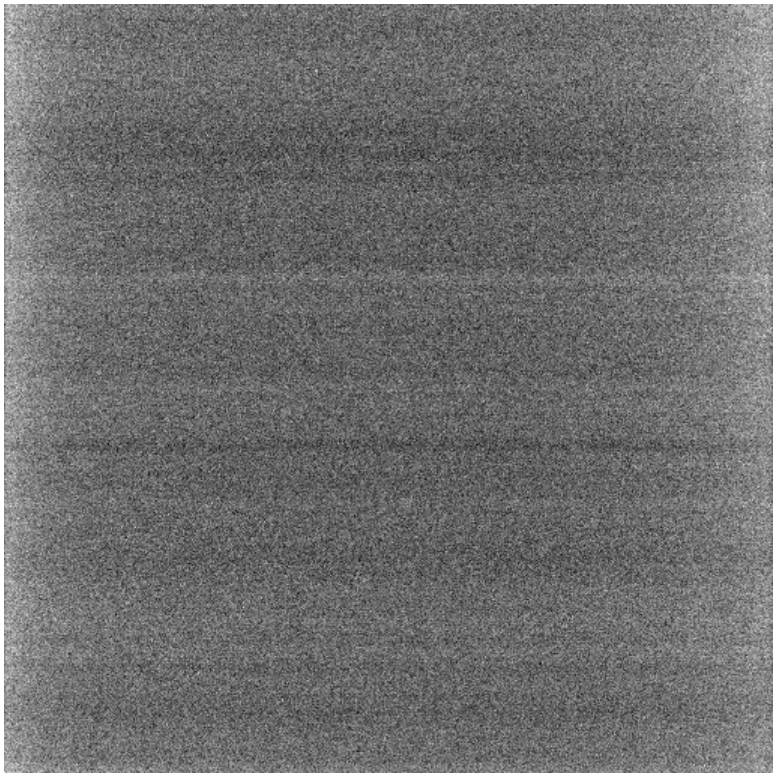

Figure 9: A median-combined full-frame image of six bias exposures. Grey-scale cuts are -6e$^-$ to +6e$^-$ relative to the bias level.

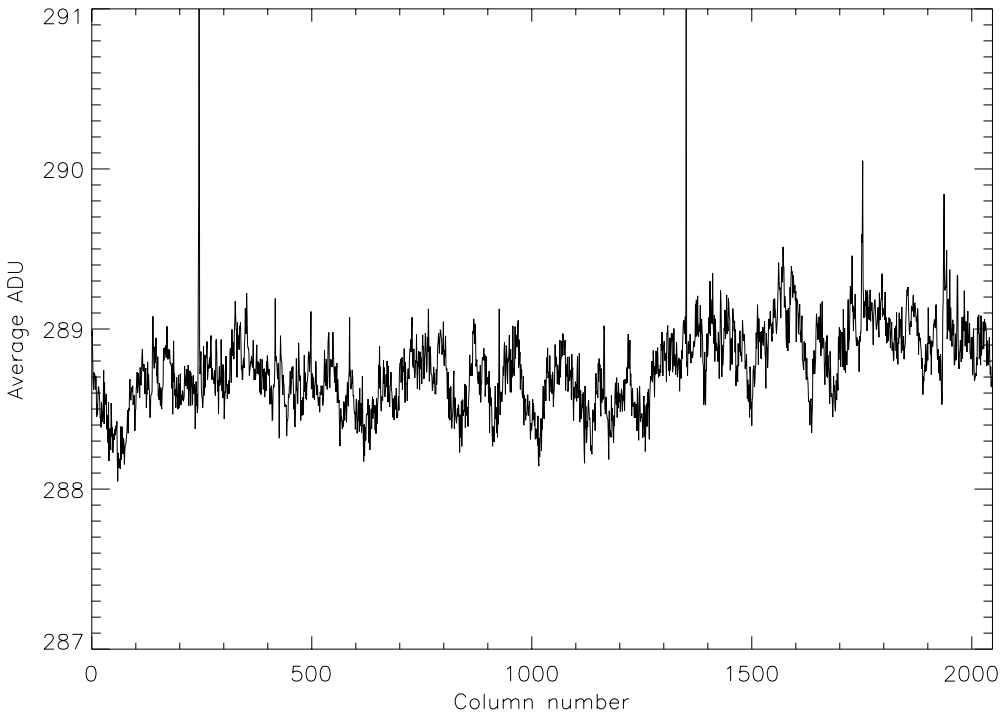

Figure 10: Vertical profile of a single bias frame.

5 Quantum-efficiency

The sensitivity has been measured through 11 narrow-band filters from 334nm to 1060nm and is plotted in figure 11. The data were extracted from an area of 400 by 400 pixels near the center of the illuminated area. The horisontal bars on the measurement points is the FWHM of the filters used.

Also shown are the room temperature test data obtained by Fairchild. The results are practically identical in the 360nm to 600nm range. At longer wavelengths, the room temperature measurements show higher QE, as the Silicon becomes less transparent. Our measurement at 334nm shows considerably higher QE than the Fairchild data. It is possible that our measurement is incorrect.

Pixel Response Non-Uniformity (PRNU) was determined from the same exposures. This is shown as vertical bars in the QE graph. Note that the PRNU amplitude shown is not scaled by the QE.

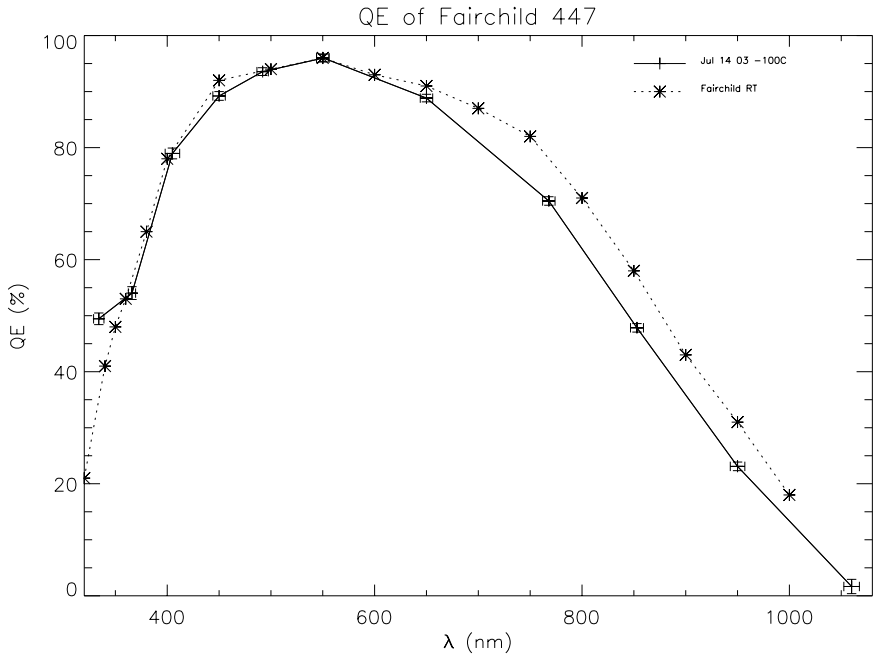

Figure 11: Global quantum efficiency versus wavelength, measured at -100°C. Also shown are Fairchild room temperature test data.

Stability of the sensitivity:

A change in QE hardly ever appears at a uniform rate over the detector. The most efficient method for checking QE instability is therefore to examine the differences in flat fields obtained some time apart. The change in local structure can be examined in figure 1 for 1060nm light, figure 2 for 550nm and figure 3 for 334nm. These flat fields were made four days apart, where the detector has been heated to room temperature and opened in between.

At 550nm and 334nm, the overall structure is unchanged, but there is a possible unstability in the centres of the low sensitivity spots. The variations seen in the ratio plots are mainly caused by a rotation of the somewhat undersized window in the test cryostat, causing differences in vignetting at the corners of the detector and movement of shadows from specks of dust on the window. Also a single dust grain appears to have landed directly on the detector surface. At 1060nm, QE again appears unchanged, but there is a change in the fringing pattern showing up in the ratio image. This is elaborated on in the section on de-lamination.

6 Fringing

At long wavelengths where the detector is partially transparent, internal reflections will create fringes, making QE change rapidly with wavelength and make the local variations strong for monochromatic light. An example flat field is shown in figure 12, illuminated by 830nm monochromatic light. The typical amplitude at this wavelength is 10%. The fringes vanish near 700nm and grows stronger toward the infrared cut-off. 830nm flat fields made before and after the de-lamination appear to be identical, as opposed to the 1060nm flat fields. This suggests that the fringes occur in a thin layer close to the surface, and is probably a result of thickness variations in the photo-sensitive layer.

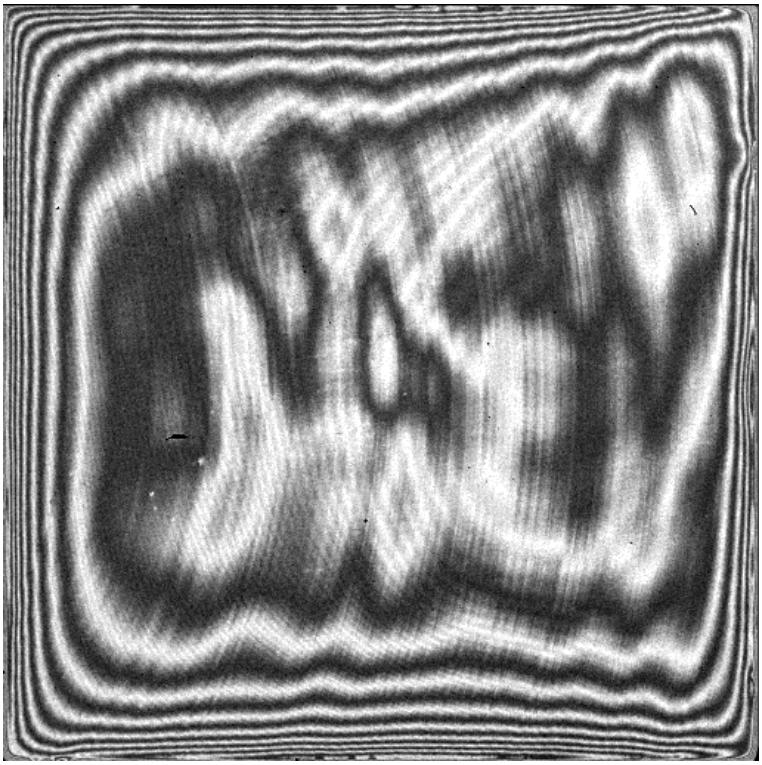

Figure 12: Fringing from 830nm laser illumination. The greyscale cuts are set to ±15% of the median level.

7 Dark current

In order to minimize dark current, the detector should be operated at a temperature of -100°C. In addition, the detector design allows for Multi-Pinned-Phase operation, which further reduces the dark current. By default, the voltages are set for MPP mode.

The dark current listed below was determined from six half-hour exposures. In MPP mode, the detection of dark current was hardly significant, at $0.6 \pm 0.3 e^-/pix/h$. No structure in the distribution could be seen.

Switching MPP off, an average dark current of $10 \pm 1 e^-/pix/h$ was recorded. Without MPP, not only does the dark current increase, but there is also considerable spatial structure, as can be seen in figure 13. During the 6 hours over which non-MPP dark current was measured, the dark current monotonically dropped from $16 e^-/pix/h$ in the first image to $8 e^-/pix/h$ in the last. This indicates that non-MPP dark current is in part caused by residual image and thereby depends on the preceding illumination.

In all, it is strongly recommended to use MPP mode.

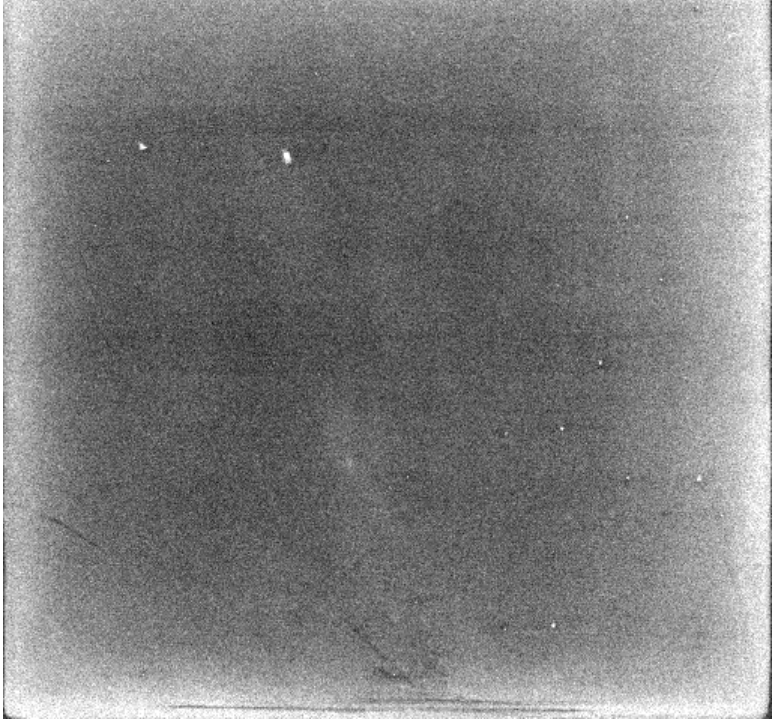

Figure 13: A median-combined full-frame image of six 30 minute dark exposures with MPP mode switched off at a detector temperature of -100°C. Grey-scale cuts are -6 / +20e^- relative to the bias level.

8 Charge Transfer Efficiency

The fraction of electrons that are successfully moved from one pixel to another during read-out is described by the charge transfer efficiency (CTE).

The CTE has been measured using a ^{55}Fe X-ray source, whose emissions generate a specific number of photo-electrons on the CCD for each detection. The read-out counts as a function of position on the CCD can then be converted to a CTE value.

The values found for the two read-out directions at a detector temperature of -100C are:

	Amplifier A	Amplifier B
Serial CTE:	0.9999974	0.9999981
Parallel CTE:	0.9999991	0.9999992

The uncertainty on the measurements is $5 \cdot 10^{-7}$.

The CTE found is very near perfect, and the difference in horisontal CTE between the two read-out directions is too slight to influence amplifier selection.

9 De-lamination of the CCD

At a late stage during the characterisation of the CCD, a shocking view awaited when opening the camera: The substrate of the CCD had detached from the Kovar package and was only held in place by the bonding wires, of which several were broken.

The CCD images obtained in the days before did contain a warning that something was wrong: When comparing 1060nm narrow-band flat-fields as shown in figure 1, the fringe pattern had shifted in certain places. As this had ben seen in a couple of other detectors before, although less pronounced, and maybe could be caused by a change in the geometry of illumination, we did not worry much about it.

As the delaminated CCD parts were packaged for return to Fairchild, the pattern of glue between the package and substrate, as shown in figure 14, was found to be matching the 1060nm

fringes. It is likely that the change in fringe pattern is related to a de-lamination in progress.

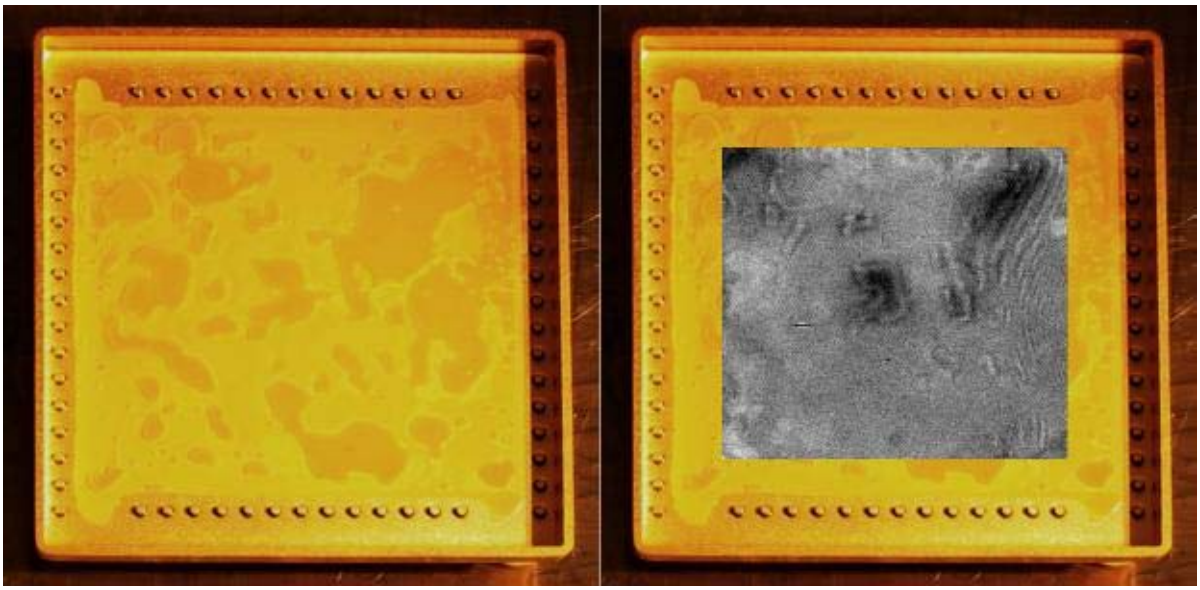

Figure 14: *Left:* Photograph of Kovar package with patches of glue. *Right:* Fringe ratio image inserted in the photograph. Note the similarity of the patterns.

After repair of the CCD package, 1060nm flatfields were obtained after every cool-down. A pair of these are displayed in figure 15, with two cooling cycles inbetween. It is hard to identify fringing in the images, and from the ratio image they appear highly similar, except for moving specks of dust. This suggests that de-lamination is not occuring now. These flatfields were made with the field lens of the FOSC camera as cryostat window, and are because of this unevenly illuminated and cannot easily be compared to the older flatfields obtained with a flat window.

10 Cryostat

The cryostat liquid Nitrogen tank is tilted relatively to the CCD to achieve an upright position when mounted on the TFOSC with the telescope pointing towards Zenith. This is done in order to maximize holding time.

Spilling will occur if the dewar is tilted shortly after filling. Filling in the morning after observations will result in the least spilling during observations. In this way, one filling per day may be sufficient.

The required time for a room-temperature camera to reach the detector operating temperature of -100°is approximately 2.5 hours.

The temperature of the cold finger sensor is about -183°C when there is LN_2 in the tank.

The pressure with a completely cooled cryostat should be approximately 10^{-6} mBar.

In a test with the cryostat flask fixed in approximately vertical position, the cold finger remained at minimum temperature until 24 hours after the previous filling of the LN2 flask. A further three hours passed until the temperature of the CCD started to climb above -100°C. I.e. the detector temperature is stable until 27 hours after LN2 filling.

When the coldfinger temperature rises, a pressure rise will occur also, and will typically reach 10^{-4} at the time where detector temperature starts to increase.

After the LN_2 is exhausted and the camera returns to room temperature, the pressure will be about 1 mBar. Evacuation before cooling again is strongly recommended.

In long dark exposures in the laboratory basement, the hit rate from energetic particles, "cosmics", was found to be 80 hits/cm^2/hour. This is a quite normal rate as expected from the natural background level, indicating that there are no significantly radioactive components in the cryostat.

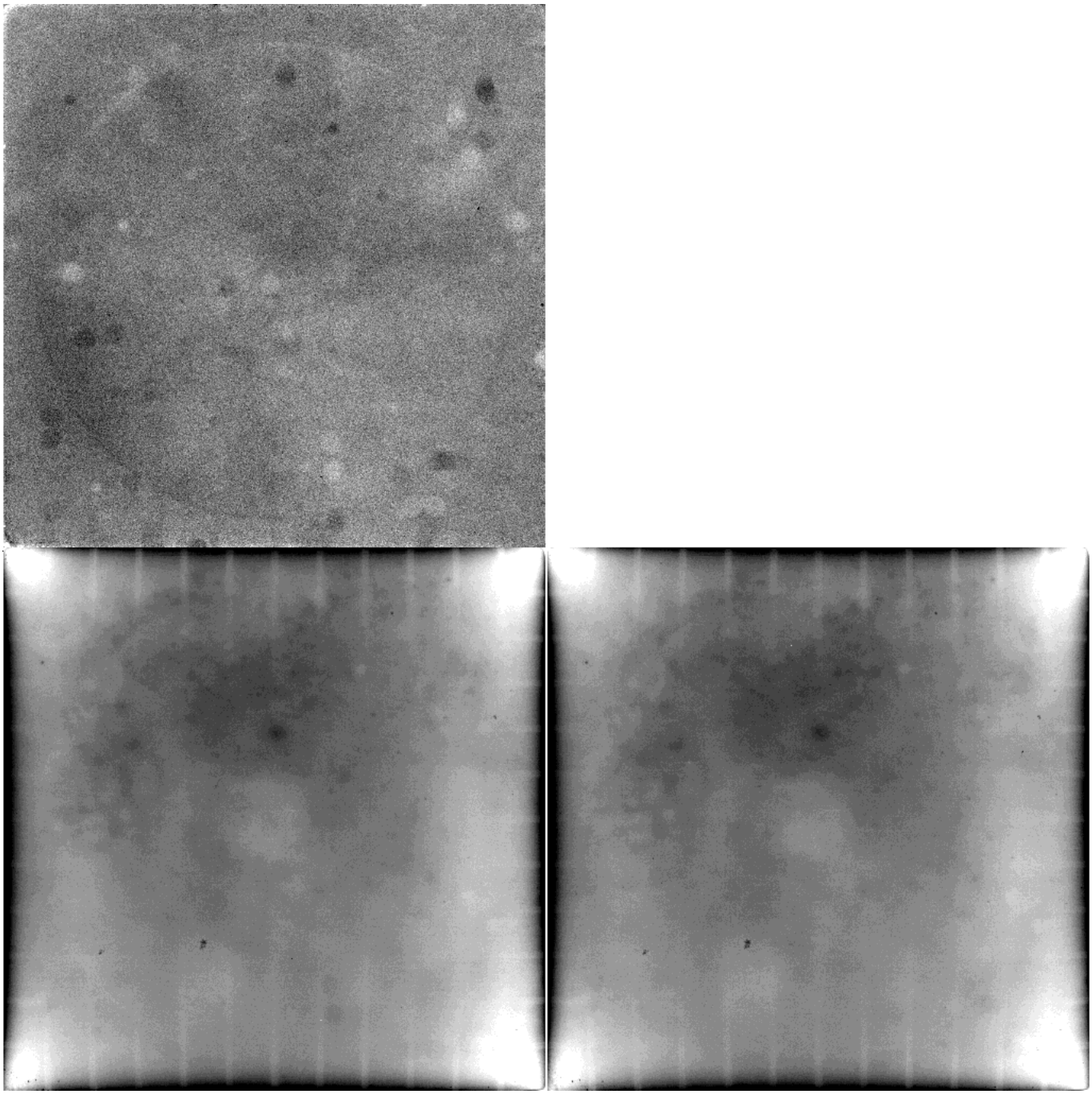

Figure 15: Flat field properties at 1060nm with field lens window, made after package repair. *Lower left:* The greyscale cuts are set to ±8% of the median level. *Lower right:* Two cooling cycles later, with identical scaling. *Top:* Ratio between the two flat fields, displayed with cuts of ±2%.